ACS APPLIED MATERIALS & INTERFACES

www.acsami.org

Research Article

Designing an Adhesive Pillar Shape with Deep Learning-Based Optimization

Yongtae Kim,[§] Charles Yang,[§] Youngsoo Kim, Grace X. Gu, and Seunghwa Ryu*

Cite This: https://dx.doi.org/10.1021/acsami.0c04123

Read Online

ACCESS | Metrics & More | Article Recommendations | Supporting Information

ABSTRACT: Over the past decades, significant effort has been made to improve the adhesive properties of adhesive pillars, by searching for pillar shapes with optimized interfacial stress distribution. However, the shape optimizations in the previous studies are conducted by considering specific pillar forms with a few parameters, hence with limited design space. In this study, we present a framework to find a free-form optimized adhesive pillar shape out of extensive design space. We generate 200 000 different shapes of adhesive pillars based on the Bézier curve with a few control points by considering two distinct edge shapes, sharp and truncated edges, to account for the limitation in the realistic manufacturing resolution. The resulting interfacial stress distributions from numerical simulations are used to train deep neural networks for each edge type. Our deep learning model shows greater than 99% classification accuracy on a limited data set with orders of magnitude speedup in computation time compared to finite element analyses. On the basis of the trained neural network, we conduct genetic optimization by maximizing a fitness function that prefers the uniform interfacial stress distribution with neither stress peak nor singularity. The optimized adhesive pillar shape is composed of smoothly mixed convex and concave parts and shows improved uniformity in the interfacial stress distribution. Our study also demonstrates that the deep learning can be used for nonparametric curve optimization task with diverse fitness function.

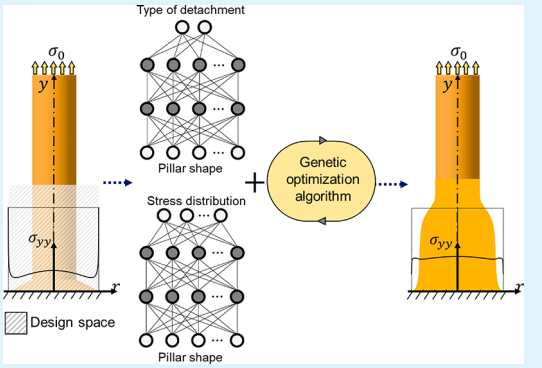

KEYWORDS: *adhesive pillar, adhesion, shape optimization, deep learning, machine learning, finite element analysis*

1. INTRODUCTION

Unlike most adhesives made of soft viscoelastic materials promoting conformal contact on a surface, biological attachment systems such as the feet of geckos, beetles, and spiders have superb and reversible adhesion properties despite their relatively stiff constituent materials such as β-keratin ($E \approx 1$ GPa).[1,2] The outstanding adhesion properties for one type of biological system (such as gecko's foot) are mainly attributed to the hierarchical fibrillary structures on the foot surface and the unique attachment/detachment mechanism.[1,3,4] Another type of attachment system does not employ such hierarchical fibrillary structure, but uses a simpler surface covered with mushroom-shaped softer microstructures which are known to reduce the stress concentration at the interface and thus show improved adhesion strength.[5] Many studies investigated bioinspired synthetic dry adhesive surfaces mimicking these microstructures for a variety of applications requiring repeatable, residue-free, and nonsticky adhesion without chemical bonds, such as reversible tapes, wall-climbing robots, grippers for transfer printing, and clean pick-and-place systems.[6−12] In addition, the polymeric dry adhesive skin patch having chemical-free adhesion and improved biocompatibility can be integrated with sensors, which offers many potential applications such as real-time health diagnostic systems.[6,13]

However, for various industrial applications, there are still challenges to be solved, such as adaptability to rough surfaces, controllability of detachment, and higher adhesion strength.[14−17] In particular, there have been numerous studies aimed at achieving higher adhesion strength with the modification of adhesive pillar.[5,18−28] The punch-shaped pillars (PSP) considered in earlier research works have relatively low adhesion strength due to the severe interfacial stress concentration at the edge region, i.e., edge stress singularity.[5,24] In the following studies, the researchers proposed a mushroom-shaped pillar in which the radius of the adhered region is larger than the radius of the stalk portion. Experimental, numerical, and theoretical studies have shown that this structure has higher adhesion strength due to the reduction of the edge stress singularity.[5,18,21,29] In addition, it is found that the edge stress singularity varies notably with the radius and thickness of tip of the mushroom-shaped pillar.[24,30] The optimization of adhesive

Received: March 3, 2020
Accepted: May 6, 2020
Published: May 6, 2020

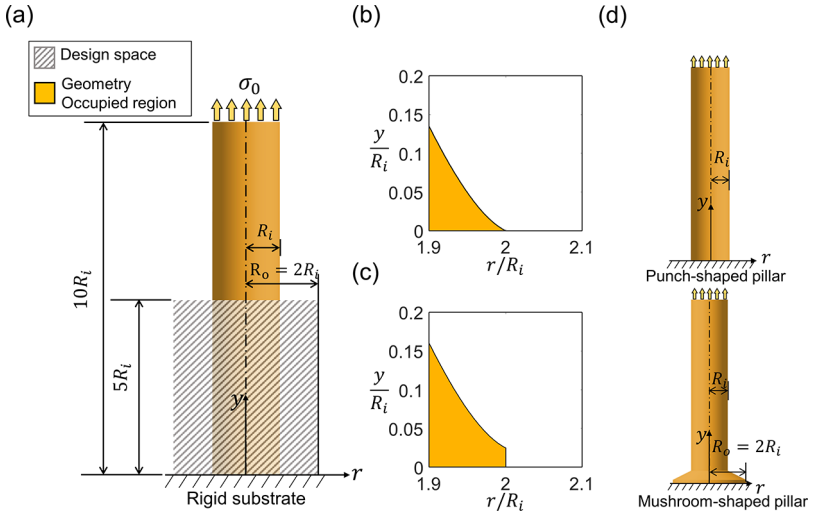

Figure 1. (a) Axial symmetric simulation model for measuring the interfacial stress distribution of the adhesive pillar. The bottom surface of the pillar is fixed to the rigid substrate with full friction contact. The explored design space is represented with a gray dashed line. The shapes of the edges are assigned to have two distinct shapes: (b) an ideally sharp edge and (c) a truncated edge considering the limitation in the fabrication technique. The sharp edge and the truncated edge have heights of 0 and $0.025R_i$ at the tip of edge, respectively. (d) The punch shaped pillar and mushroom-shaped pillar model adopted in previous studies.[28]

pillars with multiple materials is also studied by constructing gradient structure (placing softer material close to the adhesion surface of the adhesive pillar), which also shows the reduction of the edge stress singularity and the increase of the adhesion strength accompanied by the change in contact/detachment mechanism.[14,22,23,25,31] Furthermore, other researchers have proposed advanced mushroom-shaped pillars with chamfers and rounding between the stalk portion and the mushroom tip to reduce interfacial stress peaks near the transition region and edge stress singularity, which have been verified in both numerical and experimental methods.[24,26−28,32]

However, the existing studies for shape optimization of adhesive pillars are conducted in a parametric-manner and are not necessarily the global optimal shape because the design space in which the optimization proceeds is constrained by the defined design variables in the parametric functional forms.[24,27,28] In addition, it is nontrivial to use nonparametric shape optimization in conventional techniques to improve the performance of the structure by modifying its boundaries, because of its tendency to converge in a local optimum depending on the initial shape, and mechanical behavior can be sensitive to small shape changes due to the singularity or stress concentration on the structure.[33−35] Moreover, the surrogate models adapted in conventional optimizations, such as kriging, response surface method, and shallow radial basis neural network are less efficient for regression tasks involving multiple output variables (e.g., in this work, we need to train models to learn the entire stress distribution along the interface when the pillar shape is given as input) due to the relatively small numbers of fitting parameters.[36−39] It is also not straightforward to formulate the optimization process with complex objective functions subjected to constraints (e.g., we optimize the uniformity of the interfacial stress distribution with a specific type of detachment in this work.).

In this study, a nonparametric shape optimization is conducted to design adhesive pillar having high adhesion strength by maximizing the interfacial stress distribution uniformity with deep learning-based optimization, which has been recently used in various fields without the aforementioned limitation in traditional optimization techniques.[40−45] Deep neural networks (NNs) are able to efficiently learn even complex relationships from high dimensional data, unlike conventional surrogate models.[36,37] To take into account the limitation of fabrication technique such as finite spatial resolution of manufacturing methods, adhesive pillars with two distinct edge shapes, (i) ideally sharp edge and (ii) truncated edge having a certain height at the tip, are constructed. The former will give the optimal shape achievable with an ideally sharp wedge, while the latter will give the optimal shape in the presence of finite spatial resolution (such as finite resolution of additive manufacturing). We also categorize the detachment mechanisms into two types, one commencing from the edge and the other from internal region of the interface. For each edge type, we trained two different deep NNs. NNs are a computational graph of recursive, differentiable operations and update the model parameters using backpropagation to compare the model prediction with the actual target value. Deep convolutional neural networks (CNN) and deep fully connected neural networks (FCN) are adopted to classify the type of detachment mechanism and to predict interfacial stress distribution depending on the adhesive pillar shape, respectively. The trained NN allows us to accurately (and also very quickly) predict the detachment mechanism and interfacial stress distribution of a given pillar shape, without running FEM simulations. With the trained NN, the genetic optimization is performed by evolving the pool of pillar shapes at each generation into the shape having the desired detachment mechanism and interfacial stress distribution.

2. MODELING SECTION

2.1. Pillar Shape Generation. The axisymmetric pillar shapes with stalk radius (R_i) and mushroom-tip radius (R_o) are constructed as in Figure 1(a). In this work, the inverse relationship between the reduction of edge stress singularity and packing density of pillars with the change of mushroom-tip radius, the R_o are chosen to be $2R_i$.[21,30] We note that our framework can be used to obtain the optimal shape for any R_o/R_i ratio by following the procedure presented in this work. It is

https://dx.doi.org/10.1021/acsami.0c04123
ACS Appl. Mater. Interfaces XXXX, XXX, XXX−XXX

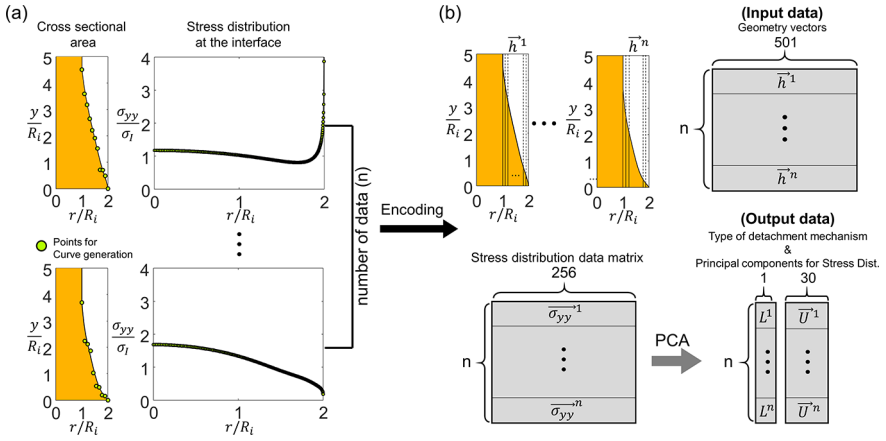

Figure 2. (a) Cross-sectional area of adhesive pillar in design space and corresponding interfacial normal stress distribution (σ_{yy}) normalized by ideal flat stress (σ_I), i.e., $\sigma_I = \sigma_0 R_o^2/R_i^2$. (b) The input of each data is formatted as the height of the adhesive pillar at a uniform interval $\Delta r/R_i = 0.002$, and outputs are formatted as 30 principal components of stress distribution and label of edge stress singularity. The numbers of input−output pairs (n) used in training our models are 98 899 and 98 143 for sharp and truncated edge types, respectively.

difficult to claim the single optimal value of the ratio, because there are pros and cons of having increased R_o/R_i, such as the inverse relationship between the reduction of edge stress singularity and packing density of pillars. A variety of smooth adhesive pillar shapes are constructed by varying the boundary shape of the adhesive pillar between the stalk and the end of mushroom-tip, based on monotonically decreasing 1st ∼10th order Bézier curve generated by 2−11 (order of the curve plus one) control points as in Figure 2(a).[46] For each edge type, we constructed 100 000 adhesive pillar models having different outer shapes: sharp edge and truncated edge, having heights of 0 and 0.025 R_i at the right end, as demonstrated in Figure 1(b) and 1(c), and obtained the corresponding interfacial normal stress distribution (σ_{yy}). The stress distribution is normalized by the ideal uniform stress distribution (σ_I) calculated as $\sigma_I = \sigma_0 R_o^2/R_i^2$. Two edge shapes are distinguished because, although the pillars with ideally sharp edges are able to completely eliminate the edge stress singularity, as shown in a previous study,[27] such an ideally sharp edge cannot be achieved in a realistic fabrication process. Also, a sharp edge can be truncated during the repeated detachment process.[26,27,47] We present the optimization results for two edge types to present both the mathematically ideal optimal shape and the optimal shape accounting for the limited resolution of a realistic fabrication process. The height of the truncated edge is chosen to present the unavoidable stress concentration in a realistic fabrication process and does not represent a specific fabrication technique.

2.2. Finite Element Analyses (FEA). For mathematical simplicity, at the interface, the relative displacement between the substrate and the pillar is assumed to be zero, as observed in experiments with adhesive pillar made polymer and rigid glass substrate,[32,47,48] and linear stress−strain relationship is assumed. We also consider the ideal rigid substrate to consider the most severe elastic modulus mismatch, i.e., infinite substrate-to-pillar modulus ratio.[49] The material properties of polydimethylsiloxane (PDMS), which is one of the most widely tested materials for adhesive pillars owing to its low surface energy and insensitive to environmental condition,[15,50] are adopted by setting Poisson's ratio (ν) = 0.49.

We applied an upward pull-off force with uniformly distributed normal stress σ_0 at the top of the pillar, and calculate the corresponding interfacial stress distribution along the pillar−substrate interface using the commercial FEM solver ABAQUS.[51] For the accurate numerical simulations, every simulation model is constructed with approximately 80 000−120 000 linear quadrilateral hybrid elements with axial symmetry, i.e., CAX4RH, and progressive fine meshes is applied near the edge to correctly account for the stress singularity.

2.3. Training Set. Considering the inevitable numerical errors from the discretization process in FEA, we eliminated the simulation results having more than 0.5% relative error between the remote pull-off force and the interfacial adhesion force (i.e., error = $|(\int_0^{2Ri} 2\pi r\sigma_{yy}\, dr - \sigma_0\pi R_i^2)/\sigma_0\pi R_i^2| \times 100\%$). The difference between the two forces should be zero in ideally accurate simulations to satisfy mechanical equilibrium conditions. However, since the error metric relies on the adhesion force and pull-off force which are obtained over the entire specimen, the local stress value may differ more than 0.5%. After eliminating some samples, we obtained 98 899 and 98 143 adhesive pillar shapes with the sharp edge and the truncated edge, respectively. We then train the NN models to predict the interfacial stress distribution and the corresponding detachment mechanism of a given pillar shape.

3. RESULTS AND DISCUSSION

3.1. Determination of Detachment Mechanism. The detachment mechanism, which affects the adhesion strength of the adhesive pillar, can be classified into three types: (i) detachment commencing near the edge due to edge stress singularity, (ii) detachment commencing within the internal region due to defects such as weak or no bonding, and (iii) fracture of the pillar in the limit of very large interfacial adhesion strength.[5,24,32] One of these detachment mechanisms initiates when the interfacial stress distribution and elastically stored energy in the pillar reach the critical condition. The adhesion strength is determined by the pull-off force measured right before any of the detachment mechanisms initiates excluding the suction and capillarity effect.[5,30,32] For example, pillar shapes having severe interfacial edge stress singularity, such as PSP, have relatively low adhesion strengths and the detachment process commences near the edge with a low pull-off force.[5,24,32,49,52] In contrary, the mushroom-shaped pillars having reduced edge stress singularity can sustain higher pull-off force in general, and if edge stress singularity reduces even further, the detachment mechanism initiates within the internal

https://dx.doi.org/10.1021/acsami.0c04123
ACS Appl. Mater. Interfaces XXXX, XXX, XXX−XXX

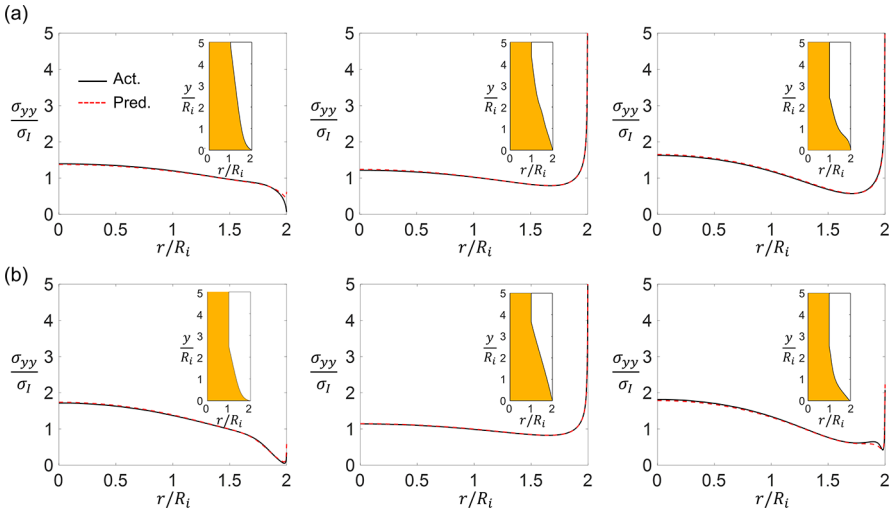

Figure 3. Comparison between predicted and actual interfacial stress distribution of randomly selected adhesive pillar with (a) sharp edge and (b) truncated edge.

interface region, not from the edge.[26,47,48,53] In some rare cases, pillar fracture can occur if the interfacial adhesion strength from the center-initiated detachment is larger than the strength of the pillar materials. The third scenario is not considered in the present study.

The adhesion strength of the adhesive pillar (S) for the edge commencing detachment mechanism can be represented with Young's modulus of pillar (E), adhesion energy (W), diameter of tip (D), and initial edge crack length (l) as follows:[49]

$$S = \frac{0.6\sqrt{EW}}{D^{0.406} l^{0.094} \tilde{a}} \tag{1}$$

where $\tilde{a}$ represents a calibration parameter representing the stress singularity in the asymptotic stress distribution near the edge obtained from numerical simulations. The adhesion strength of the mushroom shaped pillar normalized by the adhesion strength of PSP can be represented as $S/S^{\mathrm{PSP}} = \tilde{a}^{\mathrm{PSP}}/\tilde{a}$, i.e., relative ratio to the calibration parameter of PSP, $\tilde{a}^{\mathrm{PSP}}$.[22,24,49,54] However, because eq 1 cannot take into account the effect from the diverse adhesive pillar shape, we suggest a modified normalized adhesion strength for the edge commencing detachment with an effective diameter (D_{E}) as follows: $S/S^{\mathrm{punch}} = \tilde{a}^{\mathrm{PSP}} (D^{\mathrm{PSP}})^{0.406}/(\tilde{a}(D_{\mathrm{E}})^{0.406})$. Detailed explanation on the normalized strength and the calibration parameter is given in the Supporting Information (SI).

However, the adhesion strength depends not only on the edge commencing detachment but also on the internal-region commencing detachment,[5,28,48,52] and the critical value for the transition of detachment mechanism from the edge commencing to the internal-region commencing detachment mechanism is determined by the characteristics of interface, such as the roughness of surface, van der Waals interaction, and elastic mismatch between the substrate and the pillar.[15,55] It has been reported that the adhesion strength of the mushroom-shaped pillar with internal region detachment is up to 100 times larger than the adhesion strength of the PSP with edge commencing detachment.[26,30] Hence, in this work, we assume that the detachment initiates inside the internal interfacial region if the adhesion strength of a pillar determined from the edge-commencing mechanism is greater than 100 times that of PSP. If the adhesion strength is determined by the internal region commencing detachment, then the detachment can be facilitated by defects located at the interface, and if the defects are positioned within the high-stress region, then stress will be further localized and promote initiation of detachment. Furthermore, even at perfectly clean surfaces, high interfacial stresses can facilitate interfacial stress-aided thermally activated defects.[5] Taking the aforementioned mechanisms into account, one can ensure that the desired interfacial stress distribution is uniform distribution with no or small edge stress singularity. Similar arguments can also be found in the previous theoretical, numerical, and experimental studies concerning adhesive strength.[5,24,26−28,32]

3.2. Pillar Shape Optimization Combining Deep Learning and Genetic Algorithm. We perform the shape optimization for the adhesive pillar having uniform interfacial stress distribution with minimal edge singularity by employing deep learning and genetic algorithm. For the training of deep NN, the input data, which represent the shape of adhesive pillar, are formatted as 501 dimensional vectors containing the height of pillar at normalized radial positions (r/R_i) from 1 to 2, with uniform interval $\Delta r/R_i = 0.002$ (i.e., the design space is the pillar shape outside of inner radius R_i). The output data consist of two types of data processed from the interfacial stress distribution including 256 σ_{yy} values from $r/R_i = 0$ to $r/R_i = 2$ obtained with the interval, which gets gradually finer along the edge. The first type of output data is categorical data (L) representing the type of detachment mechanism. The detachment mechanism is labeled based on the edge stress singularity value as discussed in previous section; $L = 0$ for the edge-commencing mechanism if $\frac{S}{S^{\mathrm{punch}}} < 100$ and $L = 1$ for the internal region-commencing mechanism if $\frac{S}{S^{\mathrm{punch}}} \geq 100$, in one-hot binary encoding format. The second format is the dimensionally reduced data on the interfacial stress distribution based on the principal component analysis (PCA). We first construct the interfacial stress distribution matrix ($\boldsymbol{S}$) by stacking the stress distribution of each adhesive pillar in row-wise, such that the number of rows is same as the number of input configurations (i.e., 98 899 and 98 143 for sharp and truncated edges, respectively) and the number of columns is 256 σ_{yy} values along the radial direction. The stress distribution matrix is then decomposed to $\boldsymbol{S} = \boldsymbol{U}\sum\boldsymbol{V}^T$ via singular value decomposition. The cumulative explained variance (C.E.V.) with PCA is the sum of the eigenvalues

https://dx.doi.org/10.1021/acsami.0c04123
ACS Appl. Mater. Interfaces XXXX, XXX, XXX−XXX

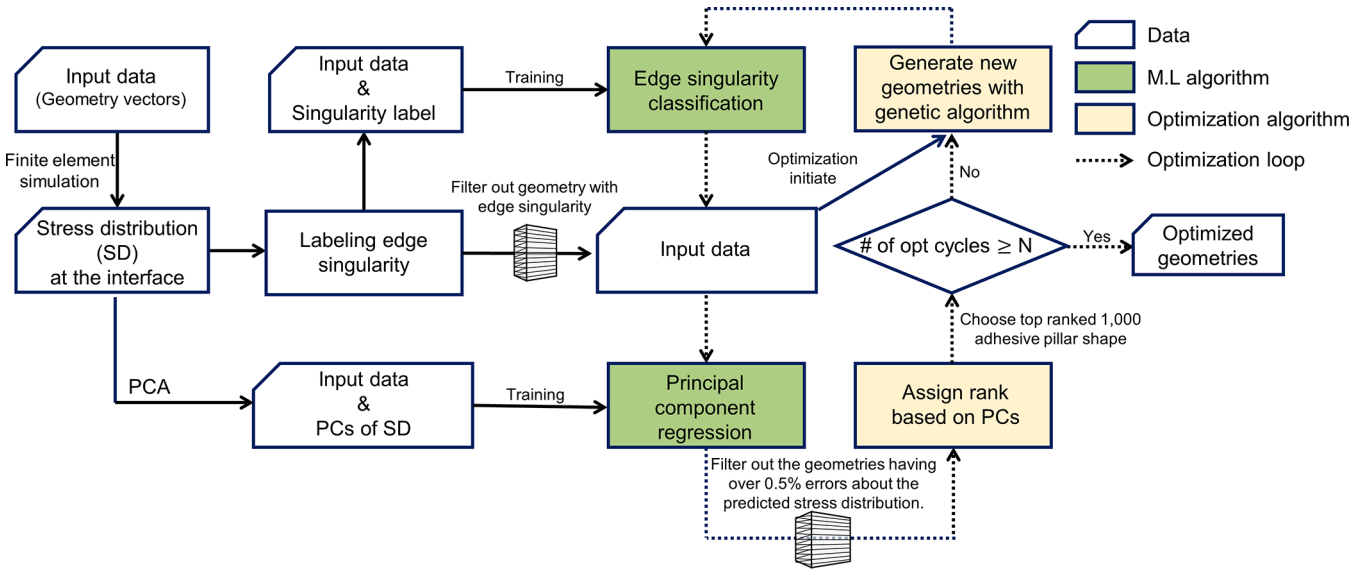

Figure 4. Overall workflow chart. The flow about data preprocessing is represented with solid arrow line, and the flow about optimization process are represented with dashed line. The geometry having over 0.5% prediction error on trained NN are eliminated during optimization process. The errors are calculated as follows: $e = |(\int_0^{2Ri} 2\pi r\sigma_{yy}\, dr - \sigma_0\pi R_i^2)/\sigma_0\pi R_i^2| \times 100\%$, i.e., the difference between the remote applied force and the interfacial adhesion force.

normalized by the sum of all eigen value, i.e., C.E.V. = $\sum_{i=1}^{n}\lambda_{ii}/\sum_{i=1}^{256}\lambda_{ii}$, and we could reduce the dimension of the interfacial stress distribution of pillar with sharp and truncated edge into 30 principal components by maintaining 99.93% and 99.88% of C.E.V., respectively. The formatting of input and output data is represented in Figure 2 (b).

Using the data as a training set, CNN are trained for the classification of the detachment mechanism, and FCN are employed for the regression of principal component values, because CNN and FCN turn out to outperform the other for the former and the latter cases, respectively. 90% of the total data are used for the training data, and the remaining 10% of the data are used as the test set. The classification accuracy for the validation set is 99.21% and 99.64% in the sharp edge and the truncated edge, respectively. We visualized the predicted and actual stress distribution of randomly chosen pillar shapes in Figure 3. The root-mean-square errors for the sharp and truncated edges turn out to be 0.0474 and 0.0300, respectively. While it takes about 3 h to obtain the interfacial stress distributions for 1000 adhesive pillar shapes with FEM simulations, the trained NN reduce the time to less than one second, which is crucial in the optimization process. The detailed information on the NN such as the architecture, training result, and the reconstruction of interfacial stress distribution from the predicted principal component can be found in the SI.

The overall flowchart of the optimization algorithm is described in Figure 4. The objective for the optimization is to find the shape of adhesive pillar having as uniform as possible interfacial stress distribution with $L = 1$ (i.e., the detachment commencing near the center), and the corresponding fitness function (f) for the genetic optimization algorithm is defined as follows:

$$f = \begin{cases} \max\left(\dfrac{\overrightarrow{\sigma_{yy}}}{\sigma_I}\right), & \text{if } L = 1 \\ \infty, & \text{if } L = 0 \end{cases} \quad (2)$$

where $\overrightarrow{\sigma_{yy}}$ and σ_I represent the normal stress distribution at the interface, and the ideal uniform stress distribution without any stress concentration at the edge, i.e., $\sigma_I = \left(\frac{R_i}{R_o}\right)^2\sigma_0$, respectively. On the basis of this fitness function, the top 1000 adhesive pillar shapes having low fitness values are selected as the mating pool containing the parent shapes for the next generation. In order to avoid a pillar shape with severe undulation, we implement the crossover with monotonically decreasing curve constraint by interpolating points between two chosen geometries, and mutation by adding noise between the two parent geometries. In addition, the new geometries based on the Bézier curve are continuously generated during each generation because the mating pool may fall into local minimum, depending on the degree of noise. Although we adapt the Bézier curve to ensure the generation of smoothly varying curves, the framework can be applied to arbitrary curve shapes. Combining these algorithms, at each generation, 11 000 geometries containing 1000 parent geometries, 9000 child geometries, and 1000 newly created geometries are generated. Because the trained NN inevitably produce the prediction error, we eliminate the shape having over 0.5% error based on the aforementioned error metric, the relative error between the remote pull-off force and interfacial adhesion force.

3.3. Optimization Results. To monitor and validate the optimization process, we plot the fitness value, i.e., $\max(\overrightarrow{\sigma_{yy}}/\sigma_I)$, by specifying the range and mean values from the top 1000 shapes generated at each generation of genetic optimization process in Figure 5. The values from the training set is plotted for the 0^{th} generation. The optimization converged in ~20 generations, and we examined 220 000 pillar shapes within less than 3 min, which is contrary to FEM simulations taking more than 3 weeks for obtaining an interfacial stress distribution about 200 000 pillar shapes. During the optimization loop, the range and mean of fitness values decrease toward the ultimate objective value of 1.

https://dx.doi.org/10.1021/acsami.0c04123
ACS Appl. Mater. Interfaces XXXX, XXX, XXX−XXX

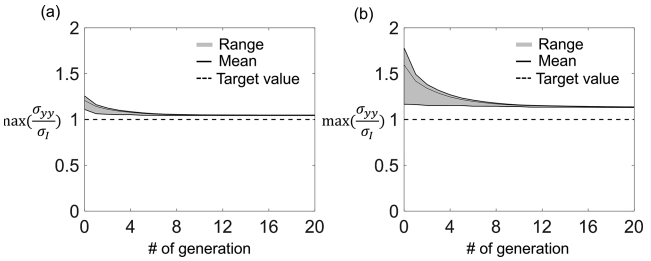

Figure 5. Evolution of fitness values of the top 1000 adhesive pillars with (a) sharp edge and (b) truncated edge at each generation during the genetic optimization. The black solid line, dashed line, and gray area represent mean of maximum interfacial stress values, i.e., $\sum_{i=1}^{1000} \max(\overrightarrow{\sigma_{yy}}^{i}/\sigma_I)/1000$, target value, and range of fitness value, respectively.

We find that the ultimate value of 1 cannot be reached even after 20 loops of the optimization, and the cause of small improvement in optimization can be mainly attributed to two reasons. First, the generated training set already has a fitness value close to objective value 1, due to the large number of training sets having very small or no interfacial stress peak. It is represented in the histogram of fitness value, which have a noticeable cluster on the value close to 1, as shown in Figure 6. In addition, in order to have internal region commencing detachment mechanism, the stress value at the edge must be diminishing, and the diminished stress should be compensated at the other interfacial region because remote pull-off force should be same as the interfacial adhesion force. Therefore, it is infeasible to reach the ultimate fitness value of 1.

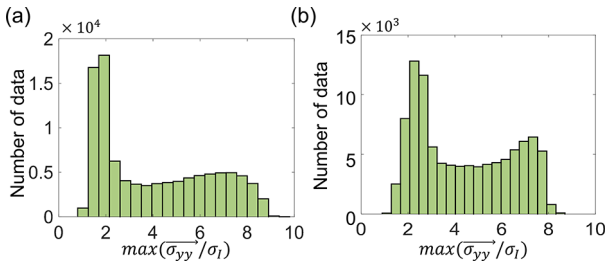

Figure 6. Histogram of $\max(\overrightarrow{\sigma_{yy}}^{i}/\sigma_I)$ about the adhesive pillars with (a) sharp edge and (b) truncated edge. The cluster on the left side and right side of the histogram about sharp edge and truncated edge represent the number of geometries having no edge stress singularity.

3.4. Discussion on the Optimal Pillar Shape. The optimal adhesive pillar shape is composed of both convex and concave region as shown in Figure 7. Such a configuration cannot be found from the simple parametric shape, e.g., chamfered or rounded transition shape from the stalk to the mushroom-tip, considered in the previous studies.[27,28] The optimized pillars with sharp edge and truncated edge are similar to each other in the most part except the region in the vicinity of the edge. In the sharp edge case, the optimized pillar shape has an overall convex curvature, and a concave shape in the vicinity of the edge with an approximately 40° angle with the substrate, because the geometry should satisfy certain geometric conditions to eliminate edge stress singularity. In contrast, the optimal pillar with a truncated edge has a flat terminal edge shape to minimize the unavoidable edge stress singularity. Because the optimization is conducted by considering the linear elastic constitutive relation, and the results are expressed with the normalized unitless value, e.g., r/R_i, the optimized shapes are size-independent. However, for realistic applications, using multiple small pillars is more advantageous than using a single large pillar owing to the increased number of contact subdivisions in multipillar arrays.[21,56] The improvement ratio, defined as $\frac{|\overline{f^{opt}} - \overline{f^{tra}}|}{\overline{f^{tra}}} \times 100\%$ where $\overline{f^{opt}}$ and $\overline{f^{tra}}$ are the averaged fitness values of the top 1000 shapes in the optimized set and the training set, are 15.4% and 40.6% in the sharp edge and the truncated edge, respectively. On the basis of the optimized pillar shape, the simulation models are constructed and tested with the direct FEM calculations. Comparison with the adhesive pillar shape optimized in a parametric manner can be found in the SI.

Although the improvement of the optimized design over the best design in the training set is small (several percent), we demonstrate that our optimization algorithm is able to converge an entire population of designs to the near-global optimal design. If we examine the best designs in the training set, then no clear design principle emerges, as they all have a variety of shapes; however, the best optimized designs all have very similar shape and curvature variation, allowing us to identify a single design that is optimal for a given problem. The comparison between the best design in the training set and the optimized-shape are included in the SI.

4. CONCLUSIONS

In this study, we obtained free-form optimized adhesive pillar shapes with two different edge shapes. The genetic optimization process is conducted with the two deep NN classifying the type

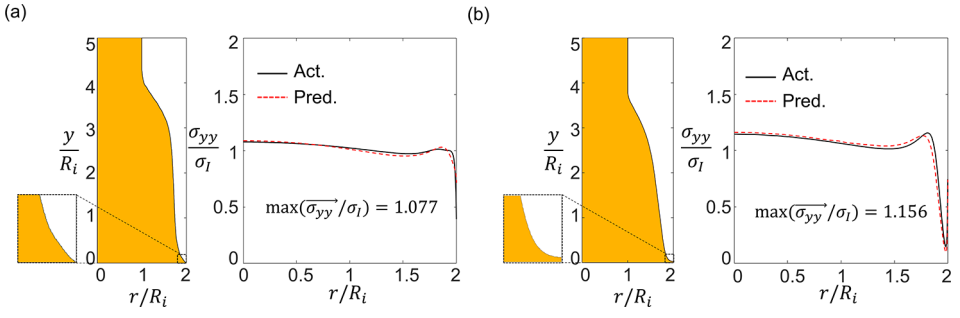

Figure 7. Optimized cross-sectional area of the adhesive pillar with (a) a sharp edge and (b) a truncated edge. The edge shapes are highlighted with the magnified view. The corresponding interfacial stress distribution is represented on the right side of each geometry. The stress values at the interface are normalized by ideal flat stress (σ_I) having no stress singularity at the edge and local stress peak.

https://dx.doi.org/10.1021/acsami.0c04123
ACS Appl. Mater. Interfaces XXXX, XXX, XXX−XXX

of detachment mechanism and predicting the interfacial stress distribution. The utilization of the deep NN is crucial in that it allows one to accurately and rapidly predict the interfacial stress distribution for a given pillar shape by learning the correlation between the high-dimensional input and output, which enables free-form optimization with a genetic algorithm. While such optimization algorithms typically require many evaluations of the pillar shape−interfacial stress distribution relationship, our deep NN is able to perform such evaluations efficiently and scalably. We find that the optimized shape is composed of smoothly varying concave and convex parts with diminishing geometries near the edge to simultaneously achieve small edge stress singularity and flat stress distribution. We were able to propose a framework to find a free-form optimized adhesive pillar shape, which was not feasible in the existing studies, and demonstrated that a single optimal design emerges from the optimization process. The proposed framework can be readily applicable to the optimization of the physical properties of various materials based on external shape tuning.

■ ASSOCIATED CONTENT

Supporting Information

The Supporting Information is available free of charge at https://pubs.acs.org/doi/10.1021/acsami.0c04123.

Details about finite element analysis; adhesion strength about the edge commencing detachment mechanism; neural networks for the classification of type of detachment mechanism and the prediction of interfacial stress distribution; comparison between the previous optimized pillar and the current optimized pillar shape; and comparison between the best design in training set and optimized shape (PDF)

■ AUTHOR INFORMATION

Corresponding Author

Seunghwa Ryu − *Department of Mechanical Engineering & KI for the NanoCentury, Korea Advanced Institute of Science and Technology (KAIST), Daejeon 34141, Republic of Korea;* orcid.org/0000-0001-9516-5809; Email: ryush@kaist.ac.kr

Authors

Yongtae Kim − *Department of Mechanical Engineering & KI for the NanoCentury, Korea Advanced Institute of Science and Technology (KAIST), Daejeon 34141, Republic of Korea*

Charles Yang − *Department of Mechanical Engineering, University of California, Berkeley, California 94720, United States*

Youngsoo Kim − *Department of Mechanical Engineering & KI for the NanoCentury, Korea Advanced Institute of Science and Technology (KAIST), Daejeon 34141, Republic of Korea*

Grace X. Gu − *Department of Mechanical Engineering, University of California, Berkeley, California 94720, United States;* orcid.org/0000-0001-7118-3228

Complete contact information is available at: https://pubs.acs.org/10.1021/acsami.0c04123

Author Contributions

§These authors contributed equally to this work.

Notes

The authors declare no competing financial interest.

■ ACKNOWLEDGMENTS

The authors acknowledge support from the Basic Science Research Program (2019R1A2C4070690) and Creative Materials Discovery Program (2016M3D1A1900038) through the National Research Foundation of Korea (NRF), as well the support of the KAIST-funded Global Singularity Research Program for 2019 (N11190118). The authors also acknowledge support from the Extreme Science and Engineering Discovery Environment (XSEDE) by National Science Foundation grant number ACI-1548562.

■ REFERENCES

(1) Heepe, L.; Gorb, S. N. Biologically inspired mushroom-shaped adhesive microstructures. *Annu. Rev. Mater. Res.* **2014**, *44*, 173−203.

(2) Autumn, K.; Liang, Y. A.; Hsieh, S. T.; Zesch, W.; Chan, W. P.; Kenny, T. W.; Fearing, R.; Full, R. J. Adhesive force of a single gecko foot-hair. *Nature* **2000**, *405* (6787), 681−685.

(3) Greiner, C.; Arzt, E.; Del Campo, A. Hierarchical gecko-like adhesives. *Adv. Mater.* **2009**, *21* (4), 479−482.

(4) Murphy, M. P.; Kim, S.; Sitti, M. Enhanced adhesion by gecko-inspired hierarchical fibrillar adhesives. *ACS Appl. Mater. Interfaces* **2009**, *1* (4), 849−855.

(5) Carbone, G.; Pierro, E.; Gorb, S. N. Origin of the superior adhesive performance of mushroom-shaped microstructured surfaces. *Soft Matter* **2011**, *7* (12), 5545−5552.

(6) Kwak, M. K.; Jeong, H. E.; Suh, K. Y. Rational design and enhanced biocompatibility of a dry adhesive medical skin patch. *Adv. Mater.* **2011**, *23* (34), 3949−3953.

(7) Song, S.; Drotlef, D.-M.; Majidi, C.; Sitti, M. Controllable load sharing for soft adhesive interfaces on three-dimensional surfaces. *Proc. Natl. Acad. Sci. U. S. A.* **2017**, *114* (22), E4344−E4353.

(8) Drotlef, D. M.; Amjadi, M.; Yunusa, M.; Sitti, M. Bioinspired composite microfibers for skin adhesion and signal amplification of wearable sensors. *Adv. Mater.* **2017**, *29* (28), 1701353.

(9) Sitti, M.; Fearing, R. S. Synthetic Gecko Foot-Hair Micro/Nano-Structures for Future Wall-Climbing Robots. In *IEEE International Conference on Robotics and Automation*, (Cat. No. 03CH37422); IEEE: 2003; pp 1164−1170.

(10) Glick, P.; Suresh, S. A.; Ruffatto, D.; Cutkosky, M.; Tolley, M. T.; Parness, A. A soft robotic gripper with gecko-inspired adhesive. *IEEE Robotics and Automation Letters* **2018**, *3* (2), 903−910.

(11) Kim, S.; Spenko, M.; Trujillo, S.; Heyneman, B.; Santos, D.; Cutkosky, M.R. Smooth vertical surface climbing with directional adhesion. *IEEE Transactions on robotics* **2008**, *24* (1), 65−74.

(12) Song, S.; Sitti, M. Soft grippers using micro-fibrillar adhesives for transfer printing. *Adv. Mater.* **2014**, *26* (28), 4901−4906.

(13) Kwak, M. K.; Pang, C.; Jeong, H. E.; Kim, H. N.; Yoon, H.; Jung, H. S.; Suh, K. Y. Towards the next level of bioinspired dry adhesives: new designs and applications. *Adv. Funct. Mater.* **2011**, *21* (19), 3606−3616.

(14) Drotlef, D.-M.; Dayan, C.; Sitti, M. Bio-inspired composite microfibers for strong and reversible adhesion on smooth surfaces. *Integr. Comp. Biol.* **2019**, *59* (1), 227−235.

(15) Li, X.; Tao, D.; Lu, H.; Bai, P.; Liu, Z.; Ma, L.; Meng, Y.; Tian, Y. Recent developments in gecko-inspired dry adhesive surfaces from fabrication to application. *Surf. Topogr.: Metrol. Prop.* **2019**, *7* (2), 023001.

(16) Murphy, M. P.; Aksak, B.; Sitti, M. Gecko-inspired directional and controllable adhesion. *Small* **2009**, *5* (2), 170−175.

(17) Boesel, L. F.; Greiner, C.; Arzt, E.; Del Campo, A. Gecko-inspired surfaces: a path to strong and reversible dry adhesives. *Adv. Mater.* **2010**, *22* (19), 2125−2137.

(18) Gorb, S. N.; Varenberg, M. Mushroom-shaped geometry of contact elements in biological adhesive systems. *J. Adhes. Sci. Technol.* **2007**, *21* (12−13), 1175−1183.

(19) Del Campo, A.; Greiner, C.; Arzt, E. Contact shape controls adhesion of bioinspired fibrillar surfaces. *Langmuir* **2007**, *23* (20), 10235−10243.
(20) Varenberg, M.; Peressadko, A.; Gorb, S.; Arzt, E. Effect of real contact geometry on adhesion. *Appl. Phys. Lett.* **2006**, *89* (12), 121905.
(21) Gorb, S.; Varenberg, M.; Peressadko, A.; Tuma, J. Biomimetic mushroom-shaped fibrillar adhesive microstructure. *J. R. Soc., Interface* **2007**, *4* (13), 271−275.
(22) Balijepalli, R. G.; Fischer, S. C.; Hensel, R.; McMeeking, R. M.; Arzt, E. Numerical study of adhesion enhancement by composite fibrils with soft tip layers. *J. Mech. Phys. Solids* **2017**, *99*, 357−378.
(23) Fischer, S. C.; Arzt, E.; Hensel, R. Composite pillars with a tunable interface for adhesion to rough substrates. *ACS Appl. Mater. Interfaces* **2017**, *9* (1), 1036−1044.
(24) Balijepalli, R.; Begley, M.; Fleck, N.; McMeeking, R.; Arzt, E. Numerical simulation of the edge stress singularity and the adhesion strength for compliant mushroom fibrils adhered to rigid substrates. *Int. J. Solids Struct.* **2016**, *85*, 160−171.
(25) Minsky, H.; Turner, K. Achieving enhanced and tunable adhesion via composite posts. *Appl. Phys. Lett.* **2015**, *106* (20), 201604.
(26) Marvi, H.; Song, S.; Sitti, M. Experimental investigation of optimal adhesion of mushroomlike elastomer microfibrillar adhesives. *Langmuir* **2015**, *31* (37), 10119−10124.
(27) Aksak, B.; Sahin, K.; Sitti, M. The optimal shape of elastomer mushroom-like fibers for high and robust adhesion. *Beilstein J. Nanotechnol.* **2014**, *5* (1), 630−638.
(28) Carbone, G.; Pierro, E. Sticky Bio-inspired Micropillars: Finding the Best Shape. *Small* **2012**, *8* (9), 1449−1454.
(29) Spuskanyuk, A.; McMeeking, R.; Deshpande, V.; Arzt, E. The effect of shape on the adhesion of fibrillar surfaces. *Acta Biomater.* **2008**, *4* (6), 1669−1676.
(30) Micciche, M.; Arzt, E.; Kroner, E. Single macroscopic pillars as model system for bioinspired adhesives: Influence of tip dimension, aspect ratio, and tilt angle. *ACS Appl. Mater. Interfaces* **2014**, *6* (10), 7076−7083.
(31) Bae, W. G.; Kim, D.; Kwak, M. K.; Ha, L.; Kang, S. M.; Suh, K. Y. Enhanced skin adhesive patch with Modulus-Tunable composite micropillars. *Adv. Healthcare Mater.* **2013**, *2* (1), 109−113.
(32) Heepe, L.; Kovalev, A. E.; Filippov, A. E.; Gorb, S. N. Adhesion Failure at 180 000 Frames per Second: Direct Observation of the Detachment Process of a Mushroom-Shaped Adhesive. *Phys. Rev. Lett.* **2013**, *111* (10), 104301.
(33) Picelli, R.; Townsend, S.; Brampton, C.; Norato, J.; Kim, H. A. Stress-based shape and topology optimization with the level set method. *Computer Methods in Applied Mechanics and Engineering* **2018**, *329*, 1−23.
(34) Shukla, A.; Misra, A. Review of optimality criterion approach scope, limitation and development in topology optimization. *Int. J. Adv. Eng. Technol.* **2013**, *6* (4), 1886.
(35) Shimoda, M.; Nagano, T.; Shi, J.-X. Non-parametric shape optimization method for robust design of solid, shell, and frame structures considering loading uncertainty. *Structural and Multidisciplinary Optimization* **2019**, *59* (5), 1543−1565.
(36) Simpson, T.; Mistree, F.; Korte, J.; Mauery, T.Comparison of Response Surface and Kriging Models for Multidisciplinary Design Optimization. In *7th AIAA/USAF/NASA/ISSMO Symposium on Multidisciplinary Analysis and Optimization*; 1998; p 4755.
(37) Hunter, D.; Yu, H.; Pukish, M. S., III; Kolbusz, J.; Wilamowski, B. M. Selection of proper neural network sizes and architectures—A comparative study. *IEEE Transactions on Industrial Informatics* **2012**, *8* (2), 228−240.
(38) Bianchini, M.; Scarselli, F. On the complexity of neural network classifiers: A comparison between shallow and deep architectures. *IEEE transactions on neural networks and learning systems* **2014**, *25* (8), 1553−1565.
(39) Liu, H.; Cai, J.; Ong, Y.-S. Remarks on multi-output Gaussian process regression. *Knowledge-Based Systems* **2018**, *144*, 102−121.
(40) Sasaki, H.; Igarashi, H. Topology Optimization Accelerated by Deep Learning. *IEEE Trans. Magn.* **2019**, *55* (6), 1−5.
(41) Gu, G. X.; Chen, C.-T.; Buehler, M. J. De novo composite design based on machine learning algorithm. *Extreme Mechanics Letters* **2018**, *18*, 19−28.
(42) Gu, G. X.; Chen, C.-T.; Richmond, D. J.; Buehler, M. J. Bioinspired hierarchical composite design using machine learning: simulation, additive manufacturing, and experiment. *Mater. Horiz.* **2018**, *5* (5), 939−945.
(43) Yu, C.-H.; Qin, Z.; Buehler, M. J. Artificial intelligence design algorithm for nanocomposites optimized for shear crack resistance. *Nano Futures* **2019**, *3* (3), 035001.
(44) Yang, C.; Kim, Y.; Ryu, S.; Gu, G. X. Using convolutional neural networks to predict composite properties beyond the elastic limit. *MRS Commun.* **2019**, *9* (2), 609−617.
(45) Yang, C.; Kim, Y.; Ryu, S.; Gu, G. X. Prediction of composite microstructure stress-strain curves using convolutional neural networks. *Mater. Des.* **2020**, *189*, 108509.
(46) Mortenson, M. E. Mathematics for computer graphics applications. *Industrial Press Inc* **1999**, No. 15, 264.
(47) Tinnemann, V.; Hernández, L.; Fischer, S. C.; Arzt, E.; Bennewitz, R.; Hensel, R. In situ observation reveals local detachment mechanisms and suction effects in micropatterned adhesives. *Adv. Funct. Mater.* **2019**, *29* (14), 1807713.
(48) Varenberg, M.; Gorb, S. Close-up of mushroom-shaped fibrillar adhesive microstructure: contact element behaviour. *J. R. Soc., Interface* **2008**, *5* (24), 785−789.
(49) Khaderi, S.; Fleck, N.; Arzt, E.; McMeeking, R. Detachment of an adhered micropillar from a dissimilar substrate. *J. Mech. Phys. Solids* **2015**, *75*, 159−183.
(50) Sameoto, D.; Menon, C. Recent advances in the fabrication and adhesion testing of biomimetic dry adhesives. *Smart Mater. Struct.* **2010**, *19* (10), 103001.
(51) Abaqus, F., Abaqus Inc.: Providence, RI, 2017.
(52) Booth, J. A.; Tinnemann, V.; Hensel, R.; Arzt, E.; McMeeking, R. M.; Foster, K. L. Statistical properties of defect-dependent detachment strength in bioinspired dry adhesives. *J. R. Soc., Interface* **2019**, *16* (156), 20190239.
(53) Heepe, L.; Varenberg, M.; Itovich, Y.; Gorb, S. N. Suction component in adhesion of mushroom-shaped microstructure. *J. R. Soc., Interface* **2011**, *8* (57), 585−589.
(54) Fleck, N. A.; Khaderi, S. N.; McMeeking, R.; Arzt, E. Cohesive detachment of an elastic pillar from a dissimilar substrate. *J. Mech. Phys. Solids* **2017**, *101*, 30−43.
(55) Hensel, R.; Moh, K.; Arzt, E. Engineering micropatterned dry adhesives: from contact theory to handling applications. *Adv. Funct. Mater.* **2018**, *28* (28), 1800865.
(56) Greiner, C.; del Campo, A.; Arzt, E. Adhesion of bioinspired micropatterned surfaces: effects of pillar radius, aspect ratio, and preload. *Langmuir* **2007**, *23* (7), 3495−3502.

https://dx.doi.org/10.1021/acsami.0c04123
ACS Appl. Mater. Interfaces XXXX, XXX, XXX−XXX